Chapter 8

Propagating MHD Waves

The terms *"waves"* and *"oscillations"* are often used interchangably, because the general wave form is often decomposed into Fourier components, each one representing an oscillatory solution, $A(\mathbf{x},t) = \sum_n A_n \exp(-i[\mathbf{kx} - \omega_n t])$. In this book we use a stricter definition, reserving the term *oscillations* only for *standing waves* with fixed nodes (§ 7), while *propagating waves* have moving nodes (Fig. 8.1). All the MHD oscillation modes we described in chapter 7 have fixed nodes, anchored at both endpoints of a coronal loop, forced by the photospheric line-tying conditions of the magnetic field, analogous to the strings of a violin. In principle, clean harmonic oscillations are only warranted if either the excitation profile along a loop matches the sine function of a harmonic wave solution, or once an initial arbitrary displacement settles into a fundamental harmonic oscillation, after the higher harmonic components are damped out. This time interval can be quite long, for instance it amounts to about 40 oscillation periods for a clarinet, as measured with a high-speed camera. Since coronal loop oscillations have been found to be strongly damped within a few oscillation periods, they probably never have sufficient time to settle into a clean harmonic eigen mode, besides the unavoidable damping due to finite dissipation. We expect a series of short-wavelength disturbances to propagate along the loop, especially when the excitation occurs at one side of a coronal loop on a time scale much shorter than the reflection time over the entire loop length. Hence, there is a gradual transition from harmonic oscillations to propagating waves, depending on the time scale and spatial symmetry of the initial displacement. In this chapter we deal exclusively with propagating waves, a field that experienced a major breakthrough after the recent *SoHO* and *TRACE* observations, including the discoveries of *EIT* (or coronal *Moreton*) waves (Thompson et al. 1998a; Wills−Davey & Thompson 1999), compressible waves in polar plumes (Ofman et al. 1997; DeForest & Gurman 1998; Ofman et al. 1999), wave trains in coronal loops (Berghmans & Clette 1999; Robbrecht et al. 2001; De Moortel et al. 2002a,b,c), as well as with the first detection of propagating wave trains during a solar eclipse (Williams et al. 2001, 2002; Pasachoff et al. 2002). Recent reviews on the subject can be found in Roberts (2000; 2002) and Roberts & Nakariakov (2003).

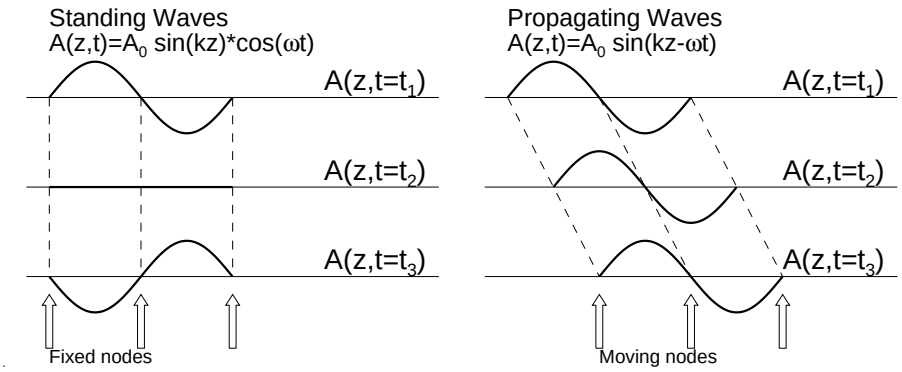

Figure 8.1: Definition of *"standing wave"* or *"oscillation"* (left) and *"propagating wave"* (right). A standing wave has fixed nodes, while a propagating wave has moving nodes as a function of time. Standing waves can also be composed by superposing two oppositely directed propagating waves.

8.1 Propagating MHD Waves in Coronal Loops

8.1.1 Evolutionary Equation for Slow-Mode MHD Waves

We derived the general dispersion relation for magneto-acoustic waves in cylindrical fluxtubes in § 7.1.4, which showed two branches of phase speed solutions ω/k: a fast-mode branch (with Alfvén speeds) and a slow-mode branch (with acoustic speeds), as shown in Fig.7.4 for coronal conditions. In this section we study the propagating waves of the slow mode for the special geometry of coronal loops, which involves gravitational stratification in the vertical direction for fluxtubes curved along closed magnetic field lines, while the case for open magnetic field lines is considered in the next section (§ 8.2). Making some simplifying assumptions, such as neglecting the coupling of the slow magneto-acoustic mode with other wave modes, 2D effects (including wave dispersion), loop curvature, whilst assuming wavelengths much shorter than the gravitational scale height, Nakariakov et al. (2000a) derived the *evolutionary equation*, using the following form of the resistive MHD equations (see § 6.1.5):

$$\frac{\partial \rho}{\partial t} + \frac{\partial}{\partial t}(\rho \mathrm{v}) = 0 \,, \tag{8.1.1}$$

$$\rho \left(\frac{\partial \mathrm{v}}{\partial t} + \mathrm{v} \frac{\partial \mathrm{v}}{\partial s} \right) = -\frac{\partial p}{\partial s} - g\rho + \frac{4}{3}\eta_0 \frac{\partial^2 \mathrm{v}}{\partial s^2} \,, \tag{8.1.2}$$

$$\frac{1}{(\gamma-1)}\frac{\partial p}{\partial t} - \frac{1}{(\gamma-1)}\frac{\gamma p}{\rho}\frac{\partial \rho}{\partial t} = \frac{\partial}{\partial s}\left(\kappa_{\parallel} \frac{\partial T}{\partial s} \right) \,, \tag{8.1.3}$$

where s is the loop length coordinate, $\rho(s)$ the plasma density, $\mathrm{v}(s)$ the longitudinal speed, $p(s)$ the plasma pressure, $T(s)$ the plasma temperature, γ the adiabatic index, $\kappa_{\parallel} = \kappa T^{5/2}$ the thermal conductivity along the magnetic field, η_0 the compressive

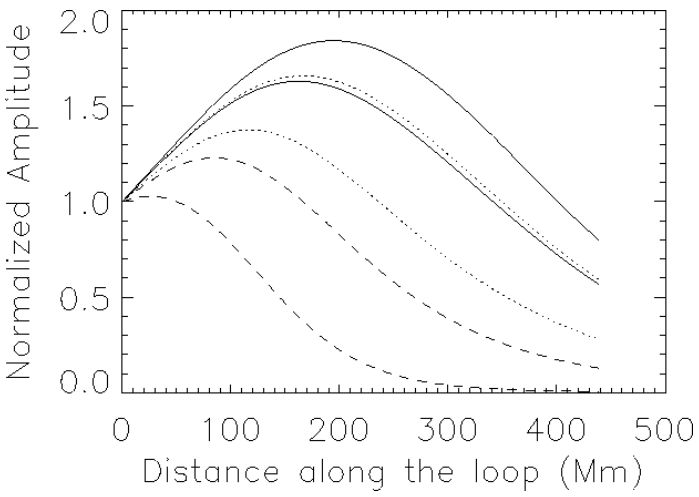

Figure 8.2: Evolution of the amplitude of slow magneto-acoustic waves with the initial amplitude $\mathrm{v}(0) = 0.02\ c_s$ for three wave periods: 900 s (solid curves), 600 s (dotted curves), and 300 s (dashed curves). The upper curve of each kind corresponds to the normalized dissipation coefficient $\overline{\eta} = 4 \times 10^{-4}$, and the lower curve to $\overline{\eta} = 4 \times 10^{-3}$. The amplitude of each wave is measured in units of the initial amplitude. The loop radius is $r_{curv} = 140$ Mm (Nakariakov et al. 2000a).

viscosity coefficient, and $g(s)$ the gravitational acceleration projected along the loop coordinate s for a semi-circular geometry (with curvature radius r_{curv}),

$$g(s) = g_\odot \cos\left(\frac{s}{r_{curv}}\right)\left(1 + \frac{r_{curv}}{R_\odot}\sin\frac{s}{r_{curv}}\right)^{-2} . \qquad (8.1.4)$$

Combining the equations (8.1.1−3) into a wave equation, Nakariakov et al. (2000a) obtained an evolutionary equation for the density perturbation in the form of a modified *Burgers equation*,

$$\frac{\partial \mathrm{v}}{\partial s} - \frac{1}{2\lambda_n}\mathrm{v} + \frac{\gamma+1}{2c_s}\mathrm{v}\frac{\partial \mathrm{v}}{\partial \xi} - \frac{R_\odot \rho_0(0)\overline{\eta}}{2\rho_0(s)}\frac{\partial^2 \mathrm{v}}{\partial \xi^2} = 0 , \qquad (8.1.5)$$

where $\xi = s - c_s t$ is the coordinate co-moving with a wave crest with sound speed c_s, $\lambda_n(s) = c_s^2(\gamma g)^{-1}$ the local density scale height, $R_{gas} = p/\rho T = 2k_B/\mu m_p$ the gas constant, and $\rho_0(0)$ the equilibrium density at the base of the corona ($s = 0$). The linearized version of Eq. (8.1.5) can be solved under the assumption of a harmonic wave, $\mathrm{v}(s) \propto \cos(k\xi) = \cos(ks - \omega t)$, propagating with sound speed $\omega/k = c_s$ with wave number k,

$$\mathrm{v}(s) = \mathrm{v}(0)\exp\left[\int_0^s \left(\frac{1}{2\lambda_n(x)} - \frac{k^2\overline{\eta}\rho_0(0)R_\odot}{2\rho_0(x)}\right)dx\right] , \qquad (8.1.6)$$

Table 8.1: Observations of slow-mode (acoustic) waves in coronal structures. N is the number of analyzed events.

Observer	N	Frequency or wavelength	Wave speed v [km/s]	Instrument
DeForest & Gurman (1998)	1	171 Å	$\approx 75 - 150$	SoHO/EIT
Berghmans & Clette (1999)	3	195 Å	$\approx 75 - 200$	SoHO/EIT
De Moortel et al. (2000b)	1	171 Å	$\approx 70 - 165$	TRACE
De Moortel et al. (2002a)	38	171 Å	122 ± 43	TRACE
De Moortel et al. (2002b)	4	195 Å	150 ± 25	TRACE
De Moortel et al. (2002c)	38	171 Å	122 ± 43	TRACE
Robbrecht et al. (2001)	4	171, 195 Å	$\approx 65 - 150$	EIT, TRACE
Berghmans et al. (2001)	1	171, 195 Å	...	EIT, TRACE
Sakurai et al. (2002)	1	5303 Å	≈ 100	Norikura
King et al. (2003)	1	171, 195 Å	...	TRACE
Marsh et al. (2003)	1	171, 368 Å	$\approx 50 - 195$	CDS, TRACE

where the normalized dissipation coefficient $\overline{\eta}$ is defined by

$$\overline{\eta} = \frac{1}{\rho_0(0) c_s R_\odot} \left[\frac{4\eta_0}{3} + \frac{\kappa_\parallel (\gamma - 1)^2}{R_{gas}\gamma} \right] . \tag{8.1.7}$$

The linearized solution of the evolutionary equation (8.1.5) yields a proportional perturbation in density, pressure, and temperature (according to the continuity equation and ideal gas equation),

$$\frac{\rho}{\rho_0} = \frac{\mathrm{v}}{c_s} , \quad \frac{p}{p_0} = \gamma \frac{\mathrm{v}}{c_s} , \quad \frac{T}{T_0} = (\gamma - 1) \frac{\mathrm{v}}{c_s} . \tag{8.1.8}$$

The evolution of each normalized quantity (Eq. 8.1.8) as a function of the loop coordinate s is shown in Fig. 8.2. The growth rate of each amplitude (in density, velocity, or pressure) is determined by the balance between the vertical gravitational stratification and dissipation (by thermal conduction and viscosity). Waves of shorter wavelengths (larger wave numbers k) grow slower than long-wavelength waves. Sufficiently short-wavelength perturbations, with $k > 1/\sqrt{\overline{\eta}\lambda_n(0)}$, do not grow at all, but decay with height. So the evolution of upward propagating slow-mode (acoustic) waves, whether they grow or decay, depends on the value of the dissipation coefficient η, thermal conduction coefficient $\kappa_\parallel$, and base density $\rho_0(0)$, as combined in the normalized dissipation coefficient $\overline{\eta}$ (Eq. 8.1.7). Nakariakov et al. (2000a) estimate a lower limit of $\overline{\eta} \approx 4 \times 10^{-4}$, using $\eta_0 = 0.352$ g cm^{-1} s^{-1} according to Braginskii's theory for $n_0 = 5 \times 10^8$ cm^{-3}, $T_e = 1.6$ MK, and neglecting thermal conduction ($\gamma = 1$). Evolutions of slow-mode acoustic waves for $\overline{\eta} = 4 \times 10^{-4}$ and 10^{-3} are shown in Fig. 8.2.

8.1.2 Observations of Acoustic Waves in Coronal Loops

Acoustic waves propagating in coronal loops were probably first noticed in EUV images of *SoHO/EIT* observations, when time sequences of flux profiles $F(s,t)$ along

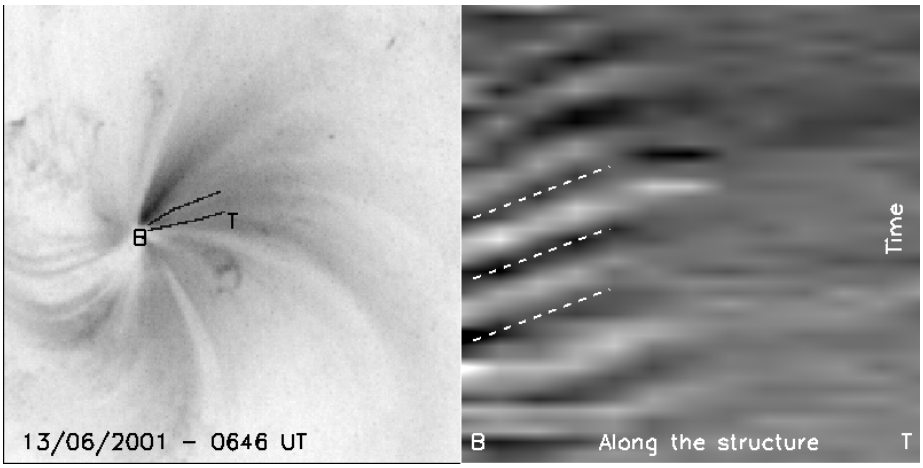

Figure 8.3: TRACE 171 Å observation of a slow-mode (acoustic) wave recorded on 2001 June 13, 06:46 UT. *Left:* the diverging fan-like loop structures emerge near a sunspot, where the acoustic waves are launched and propagate upward. *Right:* a running difference plot is shown for the loop segment marked in the left frame, with time running upward in the plot. Note the diagonal pattern which indicates propagating disturbances (De Moortel et al. 2000a).

loops with transient features were plotted with sufficiently high cadence (e.g., with $\Delta t = 15$ s, Berghmans & Clette 1999). In such space-time diagrams, diagonal patterns were noticed (e.g., Fig. 8.3 right), which exhibited slopes in the range of $\mathrm{v} = ds/dt \approx 150$ km s^{-1} (Berghmans & Clette 1999), corresponding to a speed slightly below the sound speed of $c_s \approx 180$ km s^{-1} at $T \approx 1.5$ MK expected in the used EIT 195 Å temperature band. A compilation of related observations are given in Table 8.1.

A number of propagating waves were also analyzed from TRACE data, starting in active regions and propagating upward into diverging, fan-like bundles of loops that fade out with height (Fig. 8.3, left), while no downward propagating waves were detected (De Moortel et al. 2000b, 2002a,b,c). Typical speeds of $\mathrm{v} \approx 122 \pm 43$ km s^{-1} (De Moortel et al. 2000b) were measured from TRACE 171 Å data, where the mean sound is expected to be $c_s \approx 147$ km s^{-1} at $T \approx 1.0$ MK. Multi-wavelength observations with both EIT and TRACE confirm that the diverging fan structures consist of multiple loop threads with different temperatures and corresponding sound speeds (Robbrecht et al. 2001; King et al. 2003). Time periods of $P = 172 \pm 32$ s were found for loops rooted near sunspots, which coincide with the 3-minute p-mode oscillations detected in sunspots (Brynildsen et al. 2000, 2002; Fludra 2001; Maltby et al. 2001), while waves that start further away from sunspots (in active region plages) have periods of $P = 321 \pm 74$ min, which coincide with the global 5-minute p-mode oscillations. This result clearly proves that subphotospheric acoustic p-mode oscillations penetrate through the chromosphere and transition region and excite coronal acoustic waves. The energy flux associated with these propagating waves was estimated to $d\varepsilon_{wave}/dt \approx (3.5 \pm 1.2) \times 10^2$ erg cm^{-2} s^{-1}, far below the requirement for

Table 8.2: Statistical parameters of slow-mode (acoustic) waves observed with TRACE 171 Å in 38 structures (De Moortel et al. 2002a).

Parameter	Average	Range
Length of loop segment L	26.4±9.7 Mm	10.2−49.4 Mm
Average footpoint width w	8.1±2.8 Mm	3.9−14.1 Mm
Divergence gradient dw/ds	0.28±0.16	0.07−0.71
Oscillation period P	282±93 s	145−525 s
Propagation speed v_{wave}	122±43 km/s	70−235 km/s
Wave amplitude dI/I	0.041±0.015	0.007−0.146
Brightness change I_{max}/I_{min}	7.4±5.8	1−22.7
Detection length L_{det}	8.9±4.4 Mm	2.9−23.2 Mm
Detection ratio L_{det}/L	0.367±0.188	0.08−0.814
Energy flux $d\varepsilon_{wave}/dt$	342±126 erg/(cm^2 s)	194−705 erg/(cm^2 s)

coronal heating (§ 9.1). The statistical means and ranges of the parameters measured in De Moortel et al. (2002a) are compiled in Table 8.2. The wave trains were found to fade out quickly with height, partially an effect of the decreasing flux amplitude due to the diverging geometry of the loop fans, combined with the damping caused by thermal conduction (De Moortel et al. 2002b; De Moortel & Hood 2003, 2004). The interpretation in terms of slow-mode (acoustic) waves is based on: (1) the observed propagation speed roughly corresponding to the expected sound speed in the used temperature band, and (2) slow-mode (acoustic) waves being compressional waves, producing a modulation of the density and EUV flux, and thus observed as EUV intensity modulation (which is not the case for Alfvén waves).

Slow sound waves were possibly also detected in optical wavelengths (in the green line at 5303 Å) with spectroscopic methods using the Norikura Solar Observatory, with periods of $P \approx 3-5$ min and speeds of $\mathrm{v} \approx 100$ km s^{-1} (Sakurai et al. 2002), but the confusion in white light seems to be much larger than in narrow-band EUV filters. Similarly, searches for waves with CDS data, which have substantially less spatial resolution than TRACE and EIT data, have only revealed marginal signals of oscillatory wave activity (Ireland et al. 1999; O'Shea et al. 2001; Harrison et al. 2002; Marsh et al. 2003), due to the overwhelming confusion with other spatially unresolved and time-varying loop structures.

8.1.3 Propagating Fast-Mode Waves in Coronal Loops

Fast mode MHD waves have Alfvén phase speeds, which can vary over a considerable range in coronal conditions, between the minimum Alfvén speed value v_A inside of a loop and the maximum speed v_{Ae} outside of the loop (i.e., $\mathrm{v}_A \leq \mathrm{v}_{ph} = \omega/k \leq \mathrm{v}_{Ae}$) (Fig. 7.4). We discussed the standing waves or eigen frequencies of this fast MHD wave mode in § 7.2 (kink mode) and § 7.3 (sausage mode). Now, what about propagating fast MHD waves. We quote Roberts et al. (1984): "Propagating waves, rather than standing modes, will result whenever disturbances are generated impulsively. Such waves may arise in a coronal loop, if the motions have insufficient time to reflect from the far end of

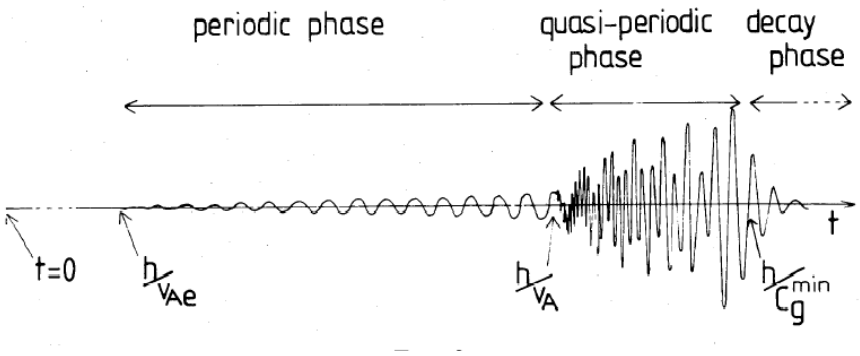

Figure 8.4: The evolution of a signal produced by a propagating fast-mode MHD wave in a coronal loop, which originates at height $h = 0$ and is observed at height $h = z$. The time intervals of the three phases depend on the characteristic velocities v_A, v_{Ae}, and c_g^{min} (Roberts et al. 1984).

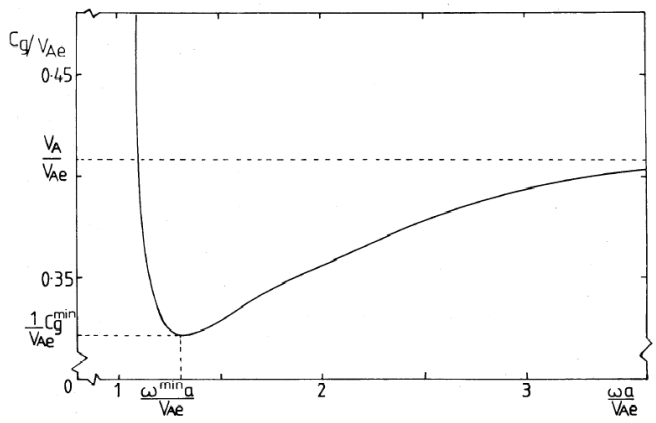

Figure 8.5: The group speed $\mathrm{v}_g = \partial\omega(k)/\partial k$, normalized by the external Alfvén velocity v_{Ae}, as a function of the dimensionless wave number frequency $k_e a = \omega a/\mathrm{v}_{Ae}$, calculated for coronal conditions $c_s \ll \mathrm{v}_A$ and $\rho_0/\rho_e = 6$. Note the occurrence of a minimum in the group speed, c_g^{min} (Roberts et al. 1984).

the loop, or in open field regions. An obvious source of such an impulsive disturbance is the flare (providing either a single or a multiple source of disturbances), but less energetic generators should not be ruled out. If the waves are generated impulsively, then the resulting disturbance may be represented as a Fourier integral over all frequencies ω and wave numbers k. In general, a wave packet results, its overall structure being determined by the dispersive nature of the modes." Roberts et al. (1984) calls this type of wave an *impulsively generated fast wave.* Such propagating fast-mode MHD waves display a bewildering variety of evolutionary scenarios, which have not been explored much in the solar context, but their hydrodynamic analogs have been widely studied in

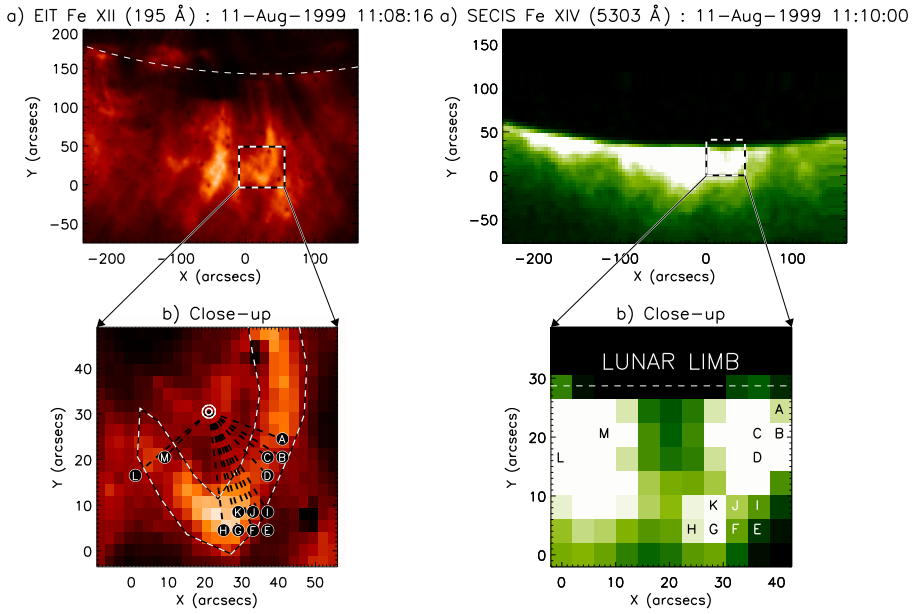

Figure 8.6: SoHO/EIT 195 Å observations (left) and *Solar Eclipse Corona Imaging System (SECIS)* observations of an active region loop during the total solar eclipse on 1999 Aug 11 (Shabla, Bulgaria), which showed propagating waves along the loop with rapid oscillations ($P = 6$ s). The SECIS image is taken in Fe XIV 5303 Å, is averaged over 50 consecutive frames (1.1 s), and is contrast-enhanced. The loop is enlarged and loop positions A−M are marked in 3×3 macropixels with a scale of $4.07''$, while the time profiles at positions A−M are shown in Fig. 8.7 (Williams et al. 2002).

oceanography. Here we summarize just some salient features as described in Roberts et al. (1984).

Let us assume that an impulsive disturbance, in the form of a magnetic field fluctuation $\mathbf{B}(z,t) = \mathbf{B}_0(z) + \mathbf{B}_1(z = z_0, t)$, launches an Alfvén wave near the footpoint of a coronal loop. As we learned in § 7.1.2, a surface wave at the boundary between the overdense loop and the less dense coronal environment will then propagate along the loop (in an upward direction), with a phase speed $\mathrm{v}_{ph} = \omega(k)/k$ that depends on the wave number k of the disturbance, which could be a broadband spectrum and excite the whole range of Alfvén velocities $\mathrm{v}_A \leq \mathrm{v}_{ph} = \omega/k \leq \mathrm{v}_{Ae}$. Let us watch the response of the loop plasma at some height $z = h$. The first signal that arrives at a height $z = h$ is that with the fastest phase speed, which is the external Alfvén speed v_{Ae}, having a frequency of $\omega_c = k_c \mathrm{v}_{Ae}$, arriving at time $t_1 = h/\mathrm{v}_{Ae}$. This is the start time of local periodic oscillations with frequency ω_c. After that, waves with slower phase speeds arrive, down to a minimum speed $\mathrm{v}_{ph} = \mathrm{v}_A$ after time $t_2 = h/\mathrm{v}_A$. This time interval $(t_1 < t < t_2)$ is called *periodic phase* (Fig. 8.4) , during which the oscillation amplitude steadily grows. However, there is a Fourier spectrum of wave frequencies ω, but the key for the understanding of the evolution is the group speed, $c_g = \partial\omega(k)/\partial k$,

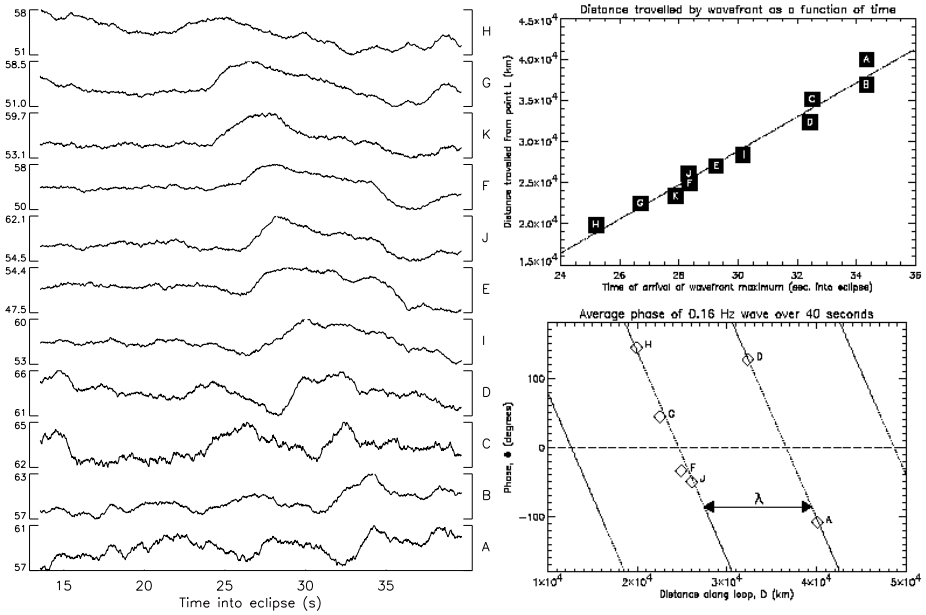

Figure 8.7: Time profiles of the intensity (left) at position A−M of the SECIS image shown in Fig. 8.6. The mean period in each time profile is $P \approx 6$ s, but the peaks shift as a function of position, indicating a propagating wave. The distance traveled by the wave maximum along the positions A−H is shown in the top right diagram, where the slope indicates a velocity of $\mathrm{v} = 2100$ km s^{-1}. The average phase as a function of the distance along the loop is shown in the bottom right diagram, yielding a wavelength of $\lambda = 12$ Mm (Williams et al. 2002).

the observed speed with which the signal of the disturbance is propagating. This group speed $\mathrm{v}_g = \partial\omega(k)/\partial k$ has a minimum value c_g^{min} at some wave vector k, as shown in Fig. 8.5, which will arrive at time $t_3 = h/c_g^{min}$ at height $z = h$. The time interval $t_2 < t < t_3$ is called the *quasi-periodic phase* (Fig. 8.4). After time t_3 the amplitude of the disturbance will decline, a phase called the *decay* (or *Airy*) phase (Fig. 8.4). These various phases of an impulsively generated fast wave have actually been observed in oceanography (Pekeris 1948). Numerical simulations of the initial stage confirm this evolutionary scenario (Murawski & Roberts 1993; 1994; Murawski et al. 1998).

The interpretation of solar observations in terms of this evolutionary scenario of fast-mode MHD waves is not trivial. Roberts et al. (1983; 1984) emphasize that the cutoff frequency ω_c and the frequency ω_{min} of the minimum group velocity c_g^{min} are the most relevant time scales to be observed and associate the periods ($P \approx 0.5 - 3.0$ s) observed in radio wavelengths to this mode of (impulsively generated) propagating fast-mode MHD waves. Propagating fast-mode MHD waves imply that a magnetic field disturbance travels at Alfvén speeds. If it modulates gyrosynchrotron emission, the corresponding radio emission should show a frequency-time drift of some ripple in the gyrosynchrotron spectrum, which perhaps has been observed in the form of a

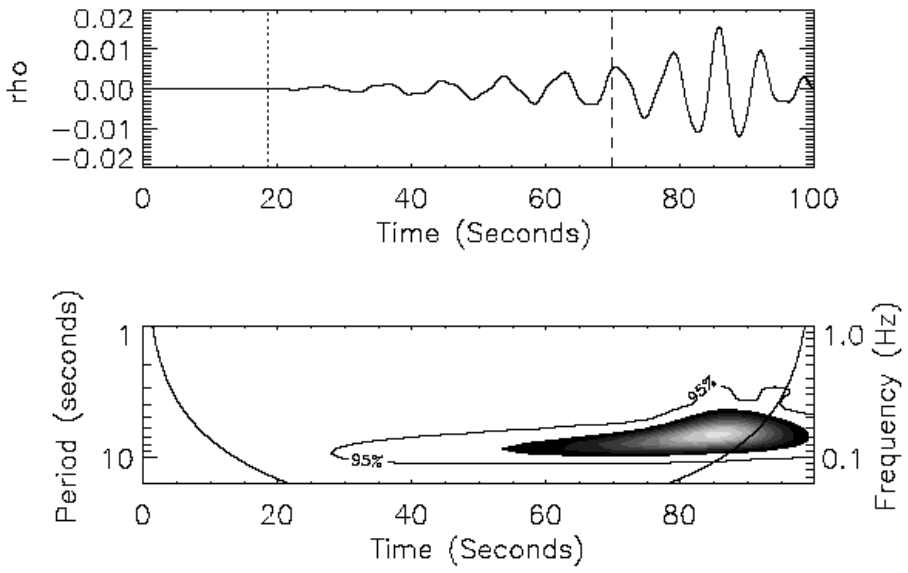

Figure 8.8: Numerical simulation of an impulsively generated fast-mode MHD wave train propagating along a corona loop with a density contrast of $\rho_0/\rho_e = 14$. *Top:* the time series is recorded at location $z = 70w$ (with w the semi-width of the loop). *Bottom:* wavelet transform analysis of the signal, exhibiting a "tadpole" wavelet signature similar to the observations shown in Fig. 8.9 (Nakariakov et al. 2003b).

quasi-periodic fine structure called *fiber bursts* (Rosenberg 1972; Bernold 1980; Slottje 1981). Most of the fast oscillation events, however, have been observed in metric and decimetric frequencies, where plasma emission dominates, but since Alfvén MHD waves are non-compressional (in contrast to the slow-mode acoustic waves), is not clear how they would modulate the plasma emission, which is only a function of the local electron density. Another problem is, even if fast-mode MHD waves modulate plasma emission, that the average density, and thus the total flux, integrated over a loop oscillating in the sausage mode would be conserved, and could not be perceived as an intensity modulation by non-imaging radio instruments, as long as they do not spatially resolve a sausage node (with spatial scale $\lambda = 2\pi/k$).

The first imaging observations that have been interpreted in terms of propagating fast-mode MHD waves (Nakariakov et al. 2003b) are the SECIS eclipse observations of Williams et al. (2001, 2002). During this eclipse, a loop has been observed with propagating wave trains in intensity, with a period of $P \approx 6$ s and a propagation speed of $\mathrm{v} \approx 2100$ km s^{-1} (Figs. 8.6 and 8.7). The evolution of the propagating fast-mode MHD oscillation has been modeled with a numeric MHD code by Nakariakov et al. (2003b), which confirmed the formation of quasi-periodic wave trains predicted by Roberts et al. (1983, 1984) and Nakariakov & Roberts (1995). The evolution of the loop density as a function of time and oscillation periods, $\rho(t, P)$ is displayed in the

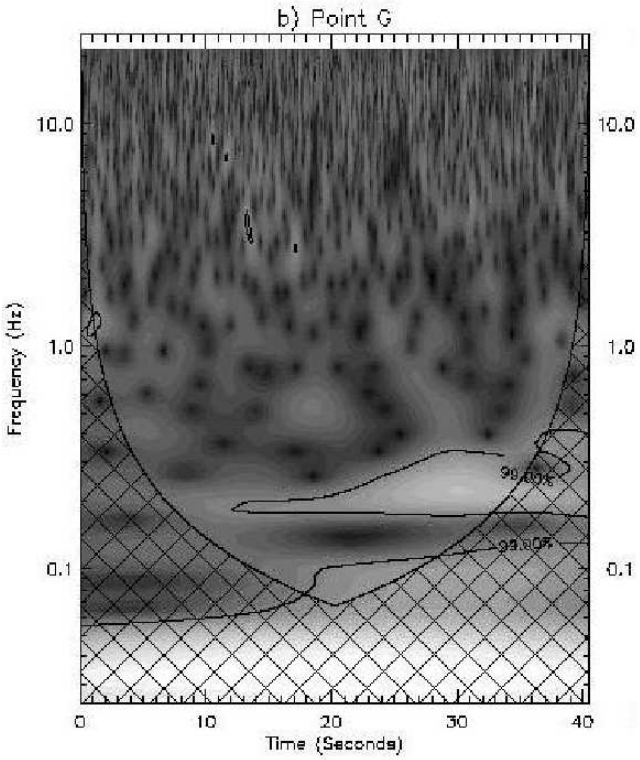

Figure 8.9: Observed wavelet transform of a coronal loop with propagating waves during the eclipse on 1999-Aug-11 observed with SECIS. Note the "tadpole" signature at $P = 1/0.16$ Hz=6 s (Katsiyannis et al. 2003).

form of a wavelet transform in Fig. 8.8, which exhibits at the dominant period $P \approx 6$ s a "tadpole" feature that is also observed by SECIS (Fig. 8.9). The SECIS observations were made with $4''$ pixels ($\approx 8''$ resolution) and averaged over 1.1 s (Katsiyannis et al. 2003). There are no detections of fast-mode MHD waves in coronal loops reported from SoHO/EIT or TRACE, probably because they are rarely operated at their highest possible cadence of seconds. We expect that more detections of fast-mode MHD waves will be accomplished with instruments of comparable spatial resolution and cadence in the future.

8.2 Propagating MHD Waves in the Open Corona

8.2.1 Evolutionary Equation of MHD Waves in Radial Geometry

While closed coronal structures have two boundaries, which control the energy balance and provide fixed nodes for standing waves, open field structures have only a single boundary where waves propagate in one direction without ever being reflected. An-

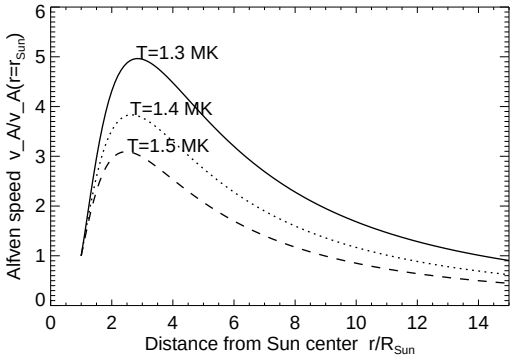

Figure 8.10: Alfvén speed as a function of radial distance from Sun center, computed for isothermal ($T_e = 1.3, 1.4, 1.5$ MK) open-field structures with radial geometry and in hydrostatic equilibrium. Note that the Alfvén speed peaks at a few solar radii.

other significant difference is the radial divergence of the open magnetic field (Fig. 1.14),

$$B_0(r) = B_0(R_\odot)\frac{R_\odot^2}{r^2}\,, \tag{8.2.1}$$

which can often be neglected in closed field structures. In an isothermal [$T(r) = const$] plasma in hydrostatic equilibrium, the density follows the same radial dependence as the pressure (i.e., $p(r) = 2n_e(r)k_BT$, Eq. 3.1.9), and thus has the radial dependence (using Eq. 3.1.15 and $r = R_\odot + h$),

$$\rho(r) = \rho_0(R_\odot)\exp\left[-\frac{R_\odot}{\lambda_p}\left(1-\frac{R_\odot}{r}\right)\right], \tag{8.2.2}$$

with λ_p the pressure scale height for a given temperature (Eq. 3.1.16). Note that the radial divergence has no effect on the pressure scale height (see also hydrostatic analogy of water vessels in Fig. 3.12). Combining Eqs. (8.2.1) and (8.2.2) yields the variation of the Alfvén speed $\mathrm{v}_A(r)$ as a function of the radial distance r from the Sun (shown in Fig. 8.10),

$$\mathrm{v}_A(r) = \frac{B_0(R_\odot)}{[4\pi\rho_0(R_\odot)]^{1/2}}\frac{R_\odot^2}{r^2}\exp\left[\frac{R_\odot}{2\lambda_p}\left(1-\frac{R_\odot}{r}\right)\right]. \tag{8.2.3}$$

In this approximation of the open magnetic field with a radial unipolar geometry, the Alfvén speed reaches a maximum at a distance of a few solar radii, while a semi-circular dipolar geometry yields a minimum in the lower corona (Fig. 5.10).

To study the propagation of magneto-acoustic waves in an open field structure with radial geometry, it is useful to transform the ideal MHD equations (§ 6.1.3) into spherical coordinates (r, θ, φ) and to choose the direction $\theta = 0$. For purely radial propagation, the ideal MHD equation in spherical coordinates can then be simplified to two uncoupled (linearized) wave equations, of which one describes Alfvén waves, characterized by magnetic perturbations B_φ and v_φ (e.g. Nakariakov et al. 2000b; Ofman et

al. 2000b; Ofman & Davila 1998; Roberts & Nakariakov 2003),

$$\frac{\partial^2 \mathrm{v}_\varphi}{\partial t^2} - \frac{B_0(r)}{4\pi\rho_0(r)r}\frac{\partial^2}{\partial r^2}[rB_0(r)\mathrm{v}_\varphi] = 0\ , \tag{8.2.4}$$

and the other describes slow-mode (acoustic) waves, characterized with density perturbations ρ and v_r,

$$\frac{\partial^2 \rho}{\partial t^2} - \frac{c_s^2}{r^2}\frac{\partial}{\partial r}\left(r^2\frac{\partial \rho}{\partial r}\right) - g(r)\frac{\partial \rho}{\partial r} = 0\ . \tag{8.2.5}$$

The right-hand side of these two equations is zero here because all dissipative effects (such as viscosity) are neglected. It is convenient to solve these two wave equations in the *Wentzel−Kramers−Brillouin (WKB)* approximation [i.e., assuming that the wavelength is much smaller than the scale of density variation of the medium ($\lambda \ll \lambda_p$)], as well as using the approximation $\lambda_p \ll R_\odot$.

In the reference frame of an upward moving Alfvén wave with local speed $\mathrm{v}_A(r)$, the transformed time variable is,

$$\tau = t - \int \frac{dr}{\mathrm{v}_A(r)}\ . \tag{8.2.6}$$

The wave equation for Alfvén waves can then be written in the WKB approximation with the variable $R = r(\lambda/\lambda_p) \ll r$,

$$\frac{d\mathrm{v}_\varphi}{dR} - \frac{R_\odot^2}{4\lambda_p R^2}\mathrm{v}_\varphi = 0\ , \tag{8.2.7}$$

which is the linearized evolutionary equation for an Alfvén wave with solution (Nakariakov et al. 2000b),

$$\mathrm{v}_\varphi(r) = \mathrm{v}_\varphi(R_\odot)\exp\left[\frac{R_\odot}{4\lambda_p}(1-\frac{R_\odot}{r})\right]\ , \tag{8.2.8}$$

which indicates an Alfvén wave amplitude that is growing with height. This has the implication that Alfvén waves can propagate large distances and deposit energy and momentum several radii away from the Sun. The growth of Alfvén waves with height has also the consequence that nonlinear effects come into play, for instance wave energy transfer of higher harmonics to shorter wavelengths, where dissipation by viscosity matters (Hollweg 1971). When the wave amplitude grows, compressional waves will be driven by Alfvén waves (Ofman & Davila 1997, 1998). Such dissipative effects, which have been neglected in the simplified wave equations [i.e., the right-hand side of Eqs. (8.2.4) and (8.2.5) are set to zero], have been included for weak nonlinearity and viscosity ν_{visc} by Nakariakov et al. (2000b), leading to a more general wave equation that is the spherical scalar form of the *Cohen−Kulsrud−Burgers equation*,

$$\frac{\partial \mathrm{v}_\varphi}{\partial R} - \frac{R_\odot^2}{4\lambda_p R^2}\mathrm{v}_\varphi - \frac{1}{4\mathrm{v}_A(\mathrm{v}_A^2 - c_s^2)}\frac{\partial \mathrm{v}_\varphi^3}{\partial \tau} - \frac{\nu_{visc}}{2\mathrm{v}_A^3}\frac{\partial^2 \mathrm{v}_\varphi}{\partial \tau^2} = 0. \tag{8.2.9}$$

An example of a typical evolution of an initially harmonic Alfvén wave during its propagation in an open radial magnetic field is shown in Fig. 8.11, showing three phases

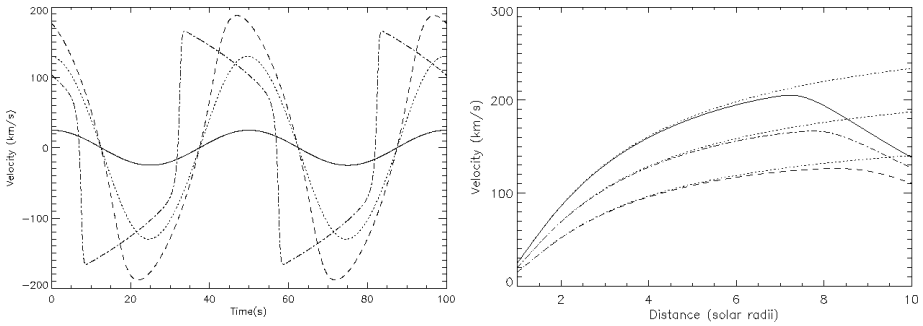

Figure 8.11: *Left:* evolution of weakly nonlinear Alfvén waves propagating in a radial magnetic field away from the Sun. The Alfvén waves have an initial speed of $\mathrm{v}_A(R_\odot = 1000$ km s$^{-1})$, an initial wave period of 50 s, an amplitude of $\mathrm{v}_\varphi = 25$ km s^{-1}, and the corona has an isothermal temperature of $T = 1.4$ MK. The evolution is shown near the Sun (solid line), at $r = 2R_\odot$ (dotted line), at $r = 5R_\odot$ (dashed line), and at $r = 9R_\odot$ dotted-dashed line. *Right:* dependence of the nonlinear spherical Alfvén wave amplitude on the distance from the Sun, for 3 different initial amplitudes: $\mathrm{v}_\varphi = 25, 20$, and 15 km s^{-1} (solid, dotted-dashed, dashed) (Nakariakov et al. 2000b).

of nonlinear evolution: (1) linear wave growth, (2) saturation and overturn, and (3) nonlinear dissipation. The theoretically predicted growth rate of Alfvén waves can be tested with observations of the evolution of line broadening as a function of height above coronal holes, assuming that the line broadening is associated with transverse motions caused by Alfvén waves.

8.2.2 Observations of Acoustic Waves in Open Corona

Probably the first detection of propagating MHD waves in (open) coronal structures was made with SoHO/EIT in 1996. Plotting the EUV brightness of polar plumes (Fig. 8.12 top) as a function of time (Fig. 8.12, bottom), using the EIT 171 Å wavelength, propagating features were noticed which had an outward speed of $\mathrm{v} \approx 75 - 150$ km s^{-1} and occurred quasi-periodically with periods of $P \approx 10 - 15$ min (DeForest & Gurman 1998). Based on the speed, which is close to the sound speed expected in this temperature band ($T \approx 1.0$ MK, $c_s = 147$ km s^{-1}), and the density modulation inferred from the EUV brightness variation, it was concluded that these wave trains in plumes correspond to propagating slow-mode magneto-acoustic waves, which are compressive waves. The energy flux associated with these wave trains was estimated to $d\varepsilon_{wave}/dt = (1.5 - 4.0) \times 10^5$ erg cm^{-2} s^{-1}, which is comparable to the heating requirement of coronal holes. The evolution of these slow-mode magneto-acoustic waves can be modeled with the theoretical wave equation (8.2.5), derived (with neglect of dissipative effects) for a radially diverging geometry, as appropriate for the these observed wave trains in polar plumes. Ofman et al. (1999) performed a numerical 2D MHD simulation of the evolution of slow-mode magneto-acoustic waves in plumes, found that the waves experience nonlinear dissipation, and concluded that they signif-

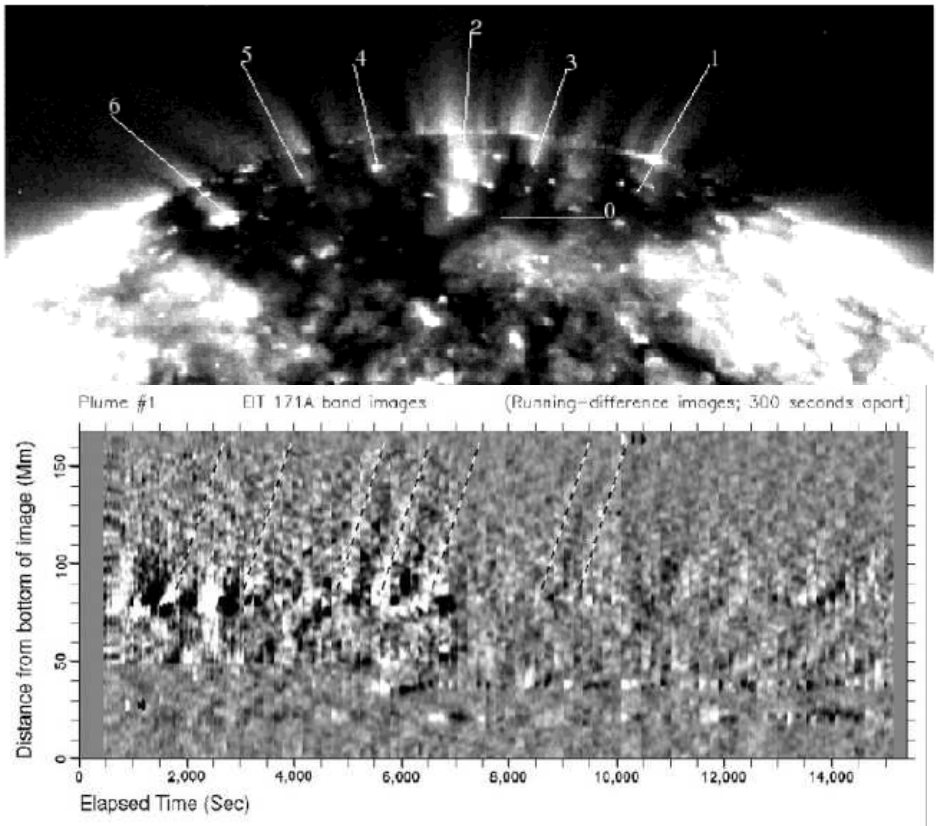

Figure 8.12: *Top:* polar plumes observed over the South Pole of the Sun with SoHO/EIT on 1996 Mar 7 at a wavelength of 171 Å, after subtraction of the radial background model. *Bottom:* running time difference images of plumes #1 and #5, with strips averaged over 360 s. Diagonal features have velocities of v ≈ 100 km s^{-1} (DeForest & Gurman 1998).

icantly contribute to the heating of the lower corona by compressive viscosity. This dissipation mechanism leads to damping of the waves within the first solar radii above the surface (Ofman et al. 2000b). Cuntz & Suess (2001) modeled slow-mode magneto-acoustic waves in plumes with a "basal-spreading" geometry and found that shocks form as a consequence at low coronal heights ($r \lesssim 1.3 R_\odot$), in contrast to models that assume weak nonlinearity.

Further away from the Sun, a search for slow-mode compressional MHD waves was carried out with the SoHO/UVCS white-light channel (Ofman et al. 1997, 2000a). Within a heliocentric distance of $r = 1.9 - 2.45\ R_\odot$, Fourier power spectra of *polarized brightness* time series revealed significant power at a period of $P \approx 6$ min (Ofman et al. 1997). A wavelet analysis of the same and additional UVCS data confirmed periods in the range of $P \approx 6 - 10$ min, with coherence times of the fluctuations over $\Delta t \approx 30$ min. Banerjee et al. (2001) found long-period oscillations in inter-plume regions with periods of $P \approx 20 - 50$ min up to a height $h \lesssim 20$ Mm above the limb, and interprets

them also as slow-mode (acoustic) waves. These observations corroborate the presence of compressional waves high above the limb, which are probably the continuation of the slow-mode magneto-acoustic waves detected in plumes with EIT.

8.2.3 Spectral Observations of Alfvén Waves in the Open Corona

After we have discovered slow-mode MHD waves in the open-field corona (e.g., in plumes, § 8.2.2), the question arises whether there also exist fast-mode MHD waves, which could provide an interesting probe for high-frequency-driven heating and acceleration of the solar wind. So far there is no direct report from imaging observations, probably because of the high time cadence and high-density contrast needed. Vertical Alfvén waves with a speed of $\mathrm{v}_A = 1000 - 10,000$ km s^{-1} would cross a vertical scale height $\lambda_n \approx 50$ Mm of the $T \approx 1.0$ MK plasma in coronal holes in $\Delta t = \lambda_n / \mathrm{v}_A = 5 - 50$ s. Moreover, Alfvén waves are non-compressional and do not modulate the plasma density, in contrast to slow-mode (acoustic) waves, while fast-mode MHD waves behave somewhere inbetween, but generally modulate the plasma density to a lesser degree than acoustic waves. On the other hand, both compressive magneto-acoustic (slow mode) and incompressive (fast-mode) Alfvén waves perturb the plasma velocity (v_1), which causes positive and negative Doppler shifts that can be detected as line broadening. If the distribution of plasma velocity perturbations is random, it broadens the natural line width in quadrature, so that the broadened line can be fitted by an effective temperature T_{eff},

$$T_{eff} = T_i + \frac{m_i}{2k_B} < \Delta \mathrm{v}^2 > , \tag{8.2.10}$$

where T_i is the temperature of line formation for an ion i, and $< \Delta \mathrm{v}^2 >$ is the average line-of-sight component of the unresolved perturbation velocities (e.g., caused by Alfvén waves).

If the line broadening $\Delta \mathrm{v}$ is caused by Alfvén waves, the theory predicts a correlation between the Alfvén velocity disturbance $\Delta \mathrm{v}(r) = \mathrm{v}_\varphi(r)$ (Eq. 8.2.8) and the mean density $\rho(r) = mn \approx m_i n_i$ (Eq. 8.2.2), which according to the evolutinary equation in radial geometry derived in § 8.2.1 is

$$\Delta \mathrm{v}(r) = \mathrm{v}_\varphi(r) \propto \rho_0^{-1/4}(r) \propto n_e^{-1/4}(r) \ . \tag{8.2.11}$$

Nonthermal broadening of UV and EUV coronal lines have been measured with *Skylab*, where nonthermal velocities of $\Delta \mathrm{v} \approx 20$ km s^{-1} were reported in coronal holes and quiet Sun regions (Doschek & Feldman 1977). More recent measurements with SoHO/SUMER (for a review see, e.g., Spadaro 1999) reveal that the nonthermal velocity increases systematically with the altitude above the limb (e.g., from $\Delta \mathrm{v} = 24$ km s^{-1} at the limb to $\Delta \mathrm{v} = 28$ km s^{-1} at a height of $h = 25$ Mm, Doyle et al. 1998), corresponding to a velocity increase that is consistent with the theoretical prediction of undamped radially propagating Alfvén waves (i.e., $[n_e(h_2)/n_e(h_1)]^{-1/4} \approx [\exp(-h/\lambda_T)]^{-1/4} = \exp(+h/4\lambda_T) \approx \exp(1/8) = 1.13$, $[(\Delta \mathrm{v}(h_2)/\Delta \mathrm{v}(h_1)] = 28/24 = 1.17$). Erdélyi et al. (1998b) detected a similar Alfvén scaling in the center-to-limb variation of the line broadening in transition region lines. Banerjee et al. (1998)

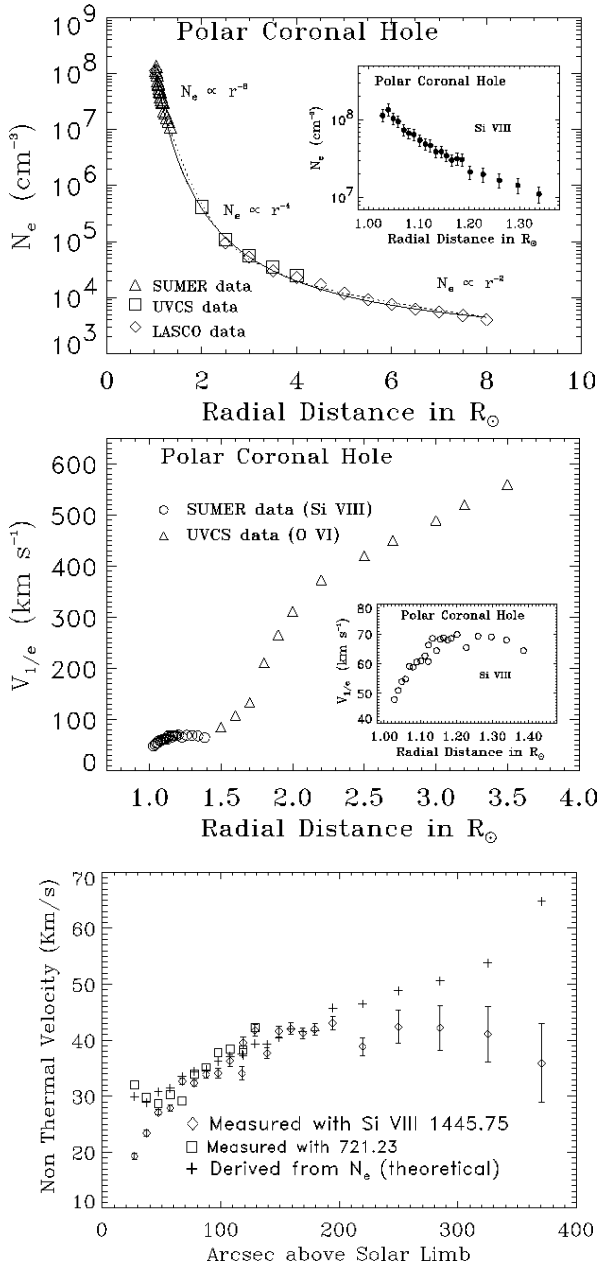

Figure 8.13: *Top:* electron density profile $n_e(h)$ above a coronal hole measured with SoHO/SUMER, UVCS, and LASCO. *Middle:* nonthermal line widths Δv measured with SUMER and UVCS. *Bottom:* comparison of measured nonthermal velocities Δv and predicted line widths from the density model $n_e(h)$ and the relation for Alfvén waves in radially diverging magnetic fields, $\Delta \mathrm{v}(h) \propto n_e^{-1/4}(r)$ (Eq. 8.2.11) (Doyle et al. 1999).

confirmed the results from Doyle et al. (1998) over a larger height range, finding an increase of the nonthermal velocity of the Si VIII line from $\Delta v(h_1) = 27$ km s^{-1} at $h_1 = 20$ Mm to $\Delta v(h_2) = 46$ km s^{-1} at $h_2 = 180$ Mm, over which range the density decreased from $n_e(h_1) = 1.1 \times 10^8$ cm^{-3} to $n_e(h_2) = 1.6 \times 10^7$ cm^{-3}; so the observed velocity increase $\Delta v(h_2)/\Delta v(h_1) = 46/27 = 1.70$ agrees well with the theoretical prediction $[n_e(h_2)/n_e(h_1)]^{-1/4} = (0.16/1.1)^{-1/4} = 1.62$. Similar nonthermal velocities were also measured by Chae et al. (1998a) with SoHO/SUMER, by Esser et al. (1999) with SoHO/UVCS (nonthermal velocity widths of $20 - 23$ km s^{-1} at $r = 1.35 - 2.1 R_\odot$), and Doschek et al. (2001) with SoHO/SUMER. Combining the Si VIII with O VI line width measurements, Doyle et al. (1999) found that the Alfvén scaling (Eq. 8.2.11) agrees well only in the height range of $h = 30 - 150$ Mm ($r = 1.04 - 1.2 R_\odot$), suggesting nonlinear evolution of the Alfvén waves at $r \gtrsim 1.2 R_\odot$ (see Fig. 8.13, bottom). Taking all these spectroscopic measurements together, there seems to be strong support for the presence of fast-mode or shear (Alfvén) MHD waves in the open field structures of the solar corona. We will discuss the relevance for coronal heating in § 9.

8.3 Global Waves

So far we have considered MHD waves that propagated inside waveguides, either in coronal loops (§ 8.1) or along vertically open structures with radial divergence (§ 8.2). However, waves have also been discovered that propagate spherically over the entire solar surface, very much like the spherical water waves you produce when you throw a stone in a pond. Obviously, the origin of these spherical waves is very localized, caused by a flare or a *coronal mass ejection (CME)* at the center of the circular waves. These global waves were first discovered in chromospheric Hα emission (called *Moreton waves*) and were recently in coronal EUV images from SoHO/EIT (called *EIT waves*). The big challenge is the physical understanding of the 3D propagation of these global waves in the complex topology of our corona, which is structured by vertical stratification, horizontal inhomogeneities, and magnetic instabilities during CMEs.

8.3.1 Moreton Waves, EIT Waves, and CME Dimming

The discovery of global waves goes back to Moreton & Ramsey (1960), who reported the finding of 7 flare events (out of 4068 flares photographed in Hα during 1959/1960) with disturbances that propagated through the solar atmosphere over distances of the order of 500,000 km at speeds of $v \approx 1000$ km s^{-1}. More such reports noted expanding arc features originating in flares and traveling distances of 200,000 km or more with lateral velocities of $v \approx 500 - 2500$ km s^{-1} (Moreton 1961; Athay & Moreton 1961; Moreton 1964; Harvey et al. 1974), or $v \approx 330 - 4200$ km s^{-1} (Smith & Harvey 1971). Reviews on early Hα observations of this type of flare waves can be found in Svestka (1976, § 4.3) and Zirin (1988; § 11). Recent observations of a Moreton wave in Hα and Hβ even revealed a velocity increase from $v = 2500$ km s^{-1} to 4000 km s^{-1} (Zhang 2001). Today it is believed, based on the high propagation speeds which are in

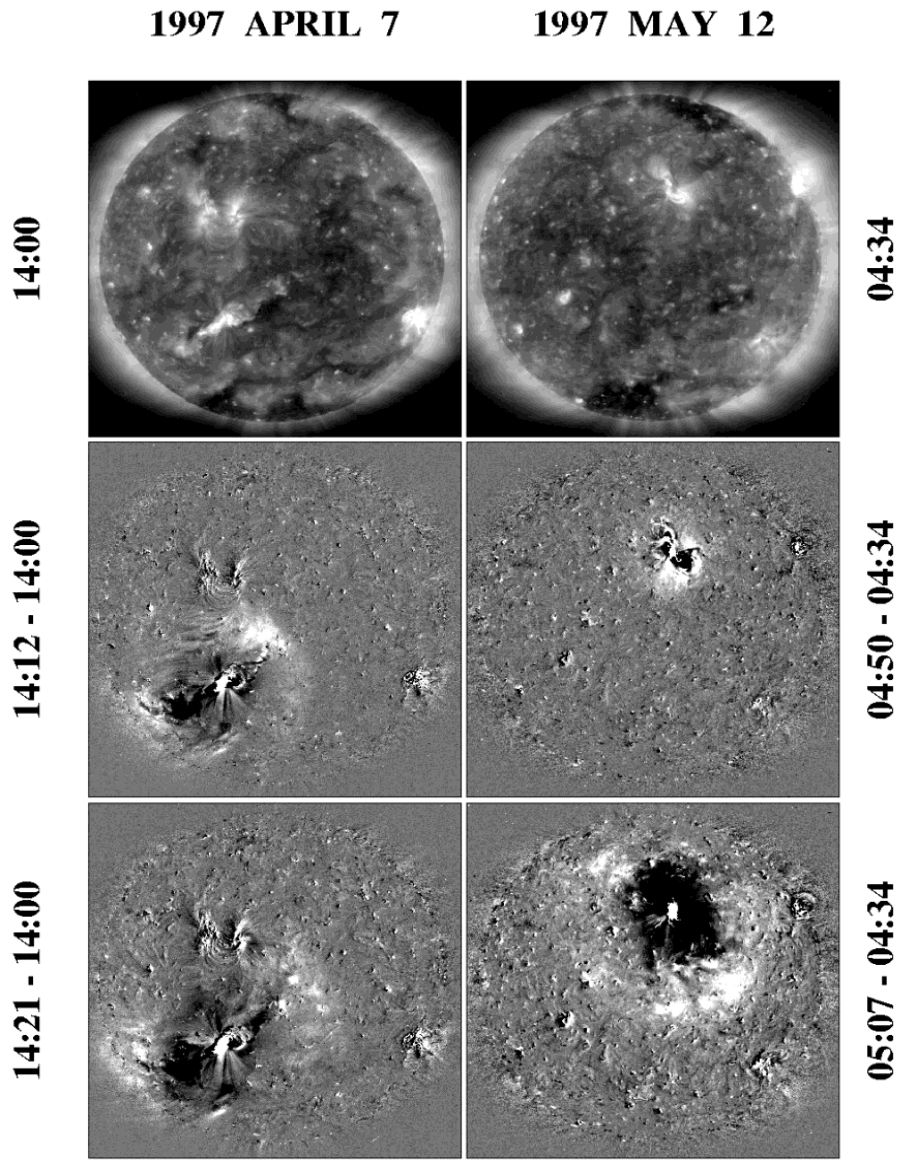

Figure 8.14: Two global wave events observed with SoHO/EIT 195 Å, on 1997 Apr 7 (left) and 1997 May 12 (right). The intensity images (top) were recorded before the eruption, while the difference images (middle and bottom) show differences between the subsequent images, enhancing emission measure increases (white areas) and dimming (black areas) (Wang 2000).

the range of coronal Alfvén speeds, that the phenomenon of Moreton waves represent a tracer of a coronal disturbance, rather than a chromospheric origin (Thompson 2001).

Recent observations by SoHO/EIT (Fig. 8.14) have provided unambiguous evi-

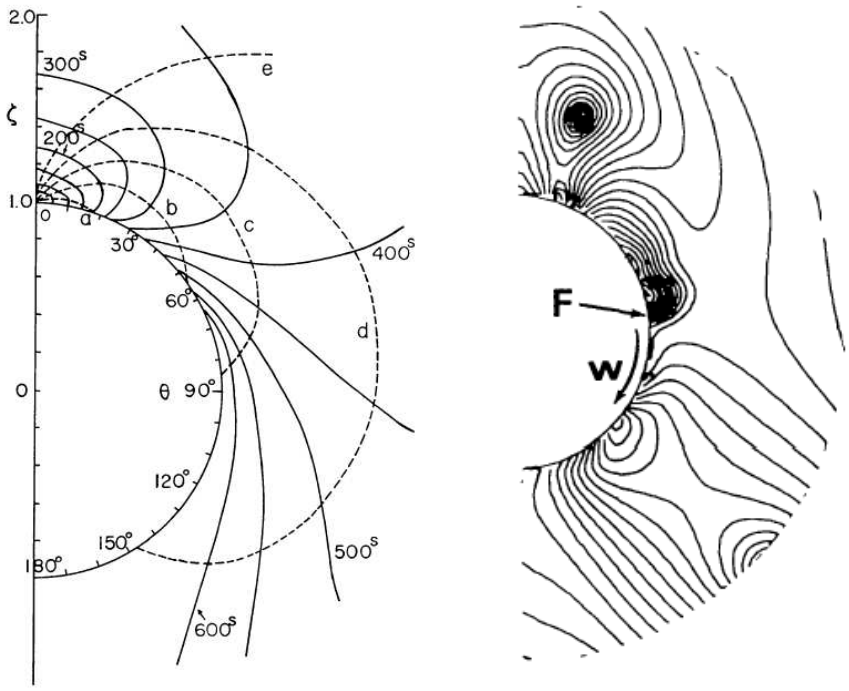

Figure 8.15: *Left:* propagation model of a Moreton wave (Uchida 1968); *Right:* iso-Alfvén speed contours calculated for a coronal portion through which a Moreton wave propagates (Uchida et al. 1973).

dence for global waves, initiated by flares and CMEs. One of the first events was observed during the Earth-directed CME of 1997-May-12, which was characterized as a bright wavefront propagating quasi-radially from the source region, leaving a dimmed region behind, and having a radial speed of $\mathrm{v} = 245 \pm 40$ km s^{-1} (Thompson et al. 1998a). More observations of such global waves followed from SoHO/EIT (Thompson et al. 1999; 2000a; Klassen et al. 2000; Biesecker et al. 2002). The catalog of 19 EIT wave events compiled by Klassen et al. (2000) investigated the correlation of radio type II events with EIT waves. Radio type II bursts are believed to trace coronal shock waves and were found to have speeds of $\mathrm{v}_{II} \approx 300 - 1200$ km s^{-1}, much faster than the EIT waves which were found to have speeds of $\mathrm{v}_{EIT} \approx 170 - 350$ km s^{-1}. Biesecker et al. (2002) investigated correlations between 175 EIT wave events and associated phenomena (CMEs, flares, and radio type II bursts). Wills−Davey & Thompson (1999) observed a global wave with a high spatial resolution using TRACE 195 Å and traced the detailed trajectories of the propagating wave fronts, finding anisotropic deviations from radial propagation and speed variations from $\mathrm{v} \approx 200$ km s^{-1} to 800 km s^{-1}, clearly illustrating the inhomogeneity of the coronal medium. Two cases of global waves have been analyzed where the wave front of Moreton waves in Hα and

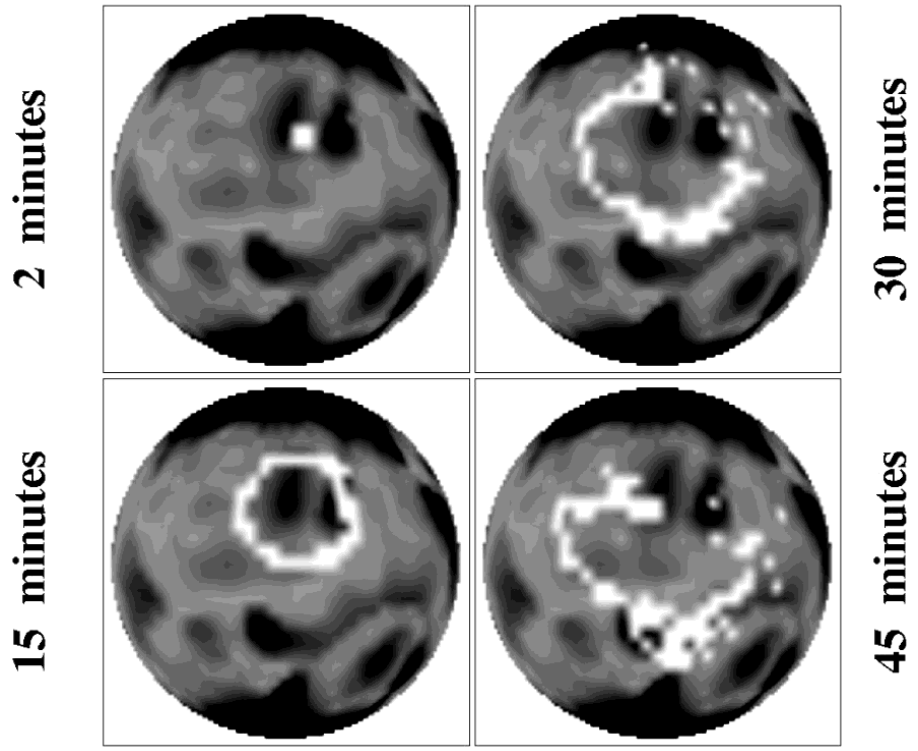

Figure 8.16: Simulation of the EIT wave event of 1997 April 7 (Fig. 8.14) by a ray-tracing method of fast-mode MHD waves. The color range indicates wave speeds $\mathrm{v} > 500$ km s^{-1} (black) and lower speeds (white). Gaps appear in the wave fronts after $t > 45$ min when waves become reflected back into the chromosphere (Wang 2000).

EIT waves were found to be co-spatial, both experiencing a subsequent deceleration, which was interpreted in terms of a fast-mode shock ("blast wave") scenario (Warmuth et al. 2001), rather than in terms of CME-associated magnetic field adjustment.

An intriguing feature of global waves seen with EIT is the dimming region (e.g., Thompson et al. 2000b), which the wave front leaves behind (see, e.g., Fig. 8.14). If the global wave would be just a compressional wave front, a density enhancement would occur at the front and a rarefaction slightly behind, while the density would be restored in the trail of the wake. The fact that a long-term dimming occurs behind the global waves indicates that material has been permanently removed behind the wave front, probably due to the vertical expulsion of the accompanying CME. This scenario is strongly supported by recent Doppler shift measurements in O V and He I, indicating vertical velocities of $\mathrm{v} = 100$ km s^{-1} in the dimming region that was feeding the CME (Harra & Sterling 2001, 2003).

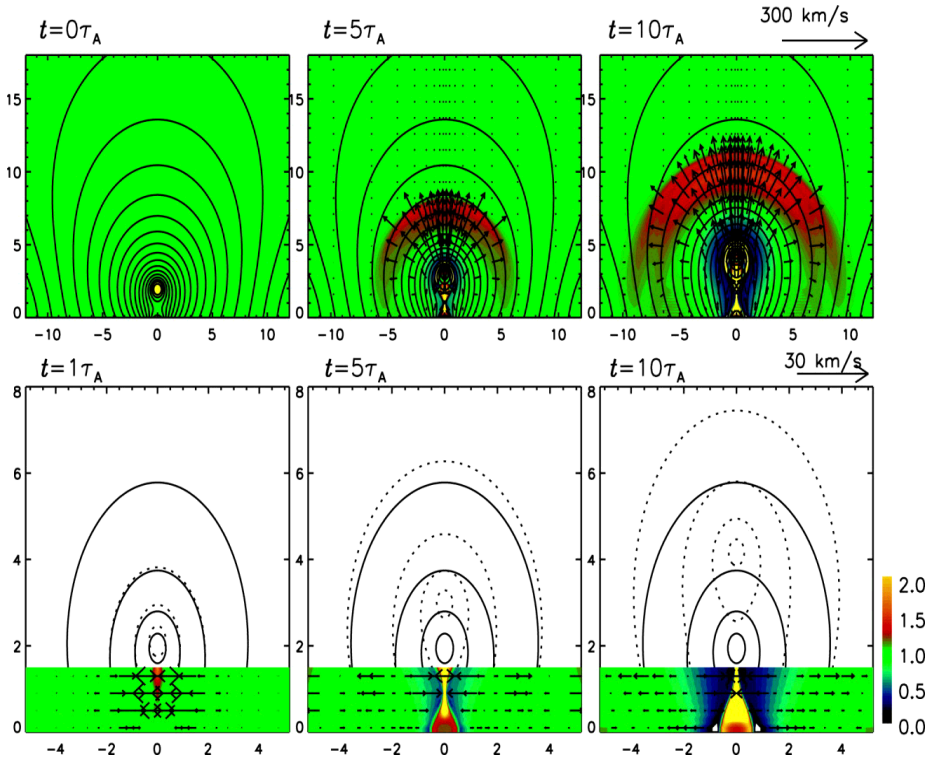

Figure 8.17: MHD simulation of a CME where a piston-driven shock forms at the envelope of the expanding CME, according to the model of Chen & Shibata 2000). The simulated case has $\beta_0 = 0.25$ and $\mathrm{v}_{rope} = 100$ km s^{-1}. *Top:* global evolution of the density (greyscale), magnetic field (solid lines), and velocity (arrows). *Lower panel:* local evolution in the lower corona and chromosphere, where the initial magnetic field is shown with solid lines (Chen et al. 2002).

8.3.2 Modeling and Simulations of Global Waves

Global waves in the solar corona were modeled early on in terms of a spherically expanding fast-mode MHD shock wave, from which the shock front is detected as an EIT wave, while the upward propagating shock is manifested in radio type II bursts (Uchida 1974), whereas the Moreton waves seen in Hα represent the chromospheric ground tracks of the dome-shaped coronal shock front (Uchida et al. 1973). Uchida (1974) derived the wave equations for such a spherically propagating fast-mode MHD wave in a radially diverging magnetic field (similar to § 8.2.1) and calculated the wave propagation in the WKB approximation (an example of a calculation of propagating wave fronts is shown in Fig. 8.15 left). Furthermore, observed electron density distributions and magnetograms were used to constrain models of the global wave propagation (Fig. 8.15 right) and the trajectories of the accompanying radio type II bursts and Moreton waves (Uchida et al. 1973; Uchida 1974). The scenario of a flare-produced initial

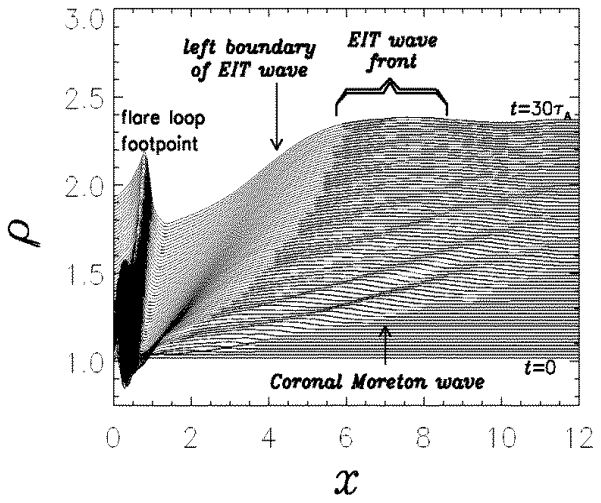

Figure 8.18: Evolution of the horizontal density $\rho(x)$ distribution obtained in the MHD simulation shown in Fig. 8.17, with an increment in time. Note the two wave features: a fast coronal Moreton wave and a slower broader EIT wave front (Chen et al. 2002).

pressure pulse that triggers a fast-mode shock propagating through the corona, the so-called *blast-wave scenario*, was further simulated with a full numerical MHD code by Steinolfson et al. (1978), the ignition of the resulting shock was modeled by Vrsnak & Lulic (2000a,b), and the formation of the expelled blobs in the coronal streamer belt were further modeled with LASCO observations by Wu et al. (2000).

A realistic numeric simulation of the EIT signature of global fast-mode MHD waves was realized by Wang (2000). Fig. 8.16 shows the result for a specific event (1997 April 7), where the global magnetic field was constrained by a photospheric magnetogram and the EUV emission by EIT 195 Å images (Fig. 8.15, left). The fast-mode MHD wave speed is defined by the dispersion relation given in Eq. (7.1.32), which has the quadratic solution (see Eq. 7.1.35 for the special case of $\theta = 0$),

$$\mathrm{v}_{ph} = \frac{1}{2}\left[\mathrm{v}_A^2 + c_s^2 + \sqrt{(\mathrm{v}_A^2 + c_s^2)^2 - 4\mathrm{v}_A^2 c_s^2 \cos^2\theta}\right] \ . \qquad (8.3.1)$$

Wang (2000) used the distribution of phase speeds $\mathrm{v}_{ph}\,[\mathbf{B}(r,\theta,\varphi)]$ constrained by the photospheric magnetic field $\mathbf{B}(r,\theta,\varphi)$ as a lower boundary condition and calculated the propagation of fast-mode wave fronts using a ray-tracing method (Fig. 8.16), which closely ressembles the observations (Fig. 8.15, left). These simulations reproduce the initial horizontal speeds of $\mathrm{v} \approx 300$ km s^{-1} of observed EIT waves, which are then found to decelerate to $\mathrm{v} = 50 - 200$ km s^{-1} in weak-field regions. The speeds simulated by Wang (2000) are consistent with the observed EIT waves, but are about $2-3$ times lower than those simulated by Uchida (1974) for Moreton waves. This discrepancy was reconciled by a numeric MHD simulation which mimics a CME by an initial strong upward-directed external force on a fluxrope, which drives the evacuation of the fluxrope with subsequent magnetic reconnection underneath (Fig. 8.17; Chen et

al. 2002; see model of Chen & Shibata 2000). A piston-driven shock appears straddling over the fluxrope, which moves upward with a super-Alfvén speed of $\mathrm{v} \approx 360$ km s^{-1}, while near the solar surface, the piston-driven shock degenerates to a finite amplitude MHD fast wave. The evolution of the horizontal density distribution is shown in Fig. 8.18, where two wave-like features are seen: (1) a piston-driven shock wave with a speed of $\mathrm{v} \approx 400$ km s^{-1}, which corresponds to the coronal Moreton wave, and (2) a second wave with an initial speed of $\mathrm{v} = 115$ km s^{-1}, which becomes increasingly blurred with time and corresponds to the EIT wave. This simulation explains the fast Moreton wave in terms of a shock wave that comes from the expanding CME, not from the flare itself, while the EIT wave front is explained in terms of an adjustment to the successive opening of CME field lines (Délannée & Aulanier 1999; Délannée 2000).

Other numerical simulations of global waves explore the stability of active regions under the impact of global waves (Ofman & Thompson 2002) or the global distribution of the coronal magnetic field (at the height of propagating EIT waves) and the coronal viscosity (Ballai & Erdélyi 2003), a new discipline that might be called *"global coronal seismology"*.

8.4 Summary

Propagating MHD waves have moving nodes, in contrast to standing modes with fixed nodes. Propagating MHD waves result mainly when disturbances are generated impulsively, on time scales faster than the Alfvén or acoustic travel time across a structure.

Propagating slow-mode MHD waves (with acoustic speed) have been recently detected in coronal loops using TRACE and EIT, usually being launched with 3-minute periods near sunspots, or with 5-minute periods away from sunspots. These acoustic waves propagate upward from a loop footpoint and are quickly damped, never being detected in downward direction at the opposite loop side. Propagating fast-mode MHD waves (with Alfvén speeds) have recently been discovered in a loop in optical (SECIS eclipse) data, as well as in radio images (from Nobeyama data).

Besides coronal loops, slow-mode MHD waves have also been detected in plumes in open field regions in coronal holes, while fast-mode MHD waves have not yet been detected in open field structures. However, spectroscopic observations of line broadening in coronal holes provide strong support for the detection of Alfvén waves, based on the agreement with the theoretically predicted scaling between line broadening and density, $\Delta \mathrm{v}(h) \propto n_e(h)^{-1/4}$.

The largest manifestation of propagating MHD waves in the solar corona are global waves that spherically propagate after a flare and/or CME over the entire solar surface. These global waves were discovered earlier in Hα, called Moreton waves, and recently in EUV, called EIT waves, usually accompanied with a coronal dimming behind the wave front, suggesting evacuation of coronal plasma by the CME. The speed of Moreton waves is about three times faster than that of EIT waves, which still challenges dynamic MHD models of CMEs.